Accepted for publication in ApJ

Stellar orbits in triaxial clusters around black holes in galactic nuclei

Niranjan Sambhus
nbs@iucaa.ernet.in

and

S. Sridhar
sridhar@iucaa.ernet.in
Inter-University Centre for Astronomy and Astrophysics
Ganeshkhind, Pune 411 007, INDIA

ABSTRACT

We investigate the orbital structure of a model triaxial star cluster, centered around a supermassive black hole (BH), appropriate to galactic nuclei. Sridhar and Touma (1999) proved that the presence of the BH enforces some regularity in the dynamics within the radius of influence of the BH. We employ their averaging method to reduce the degrees of freedom from three to two. Numerical orbit integrations, together with Poincaré surfaces of section allow us to draw a global portrait of the orbital structure; in our calculations we employ a model cluster potential that is triaxial and harmonic. The averaged dynamics of the axisymmetric case is integrable, and we present a detailed comparison of orbits in oblate and prolate axisymmetric potentials. Both cases support resonant orbits with fixed values of eccentricity, inclination, and periapse, whose lines of nodes rotates steadily. We then systematically explore significantly triaxial potentials, possessing small oblateness, or prolateness. Resonant orbits and their families are studied both numerically, and through secular perturbation theory. Chaos appears to be suppressed for all the cases we studied, and we obtain effective third integrals. Some of the orbits appear to reinforce the shape of the potential; we provide phase space, as well as real space portraits of these orbits. A particularly promising resonant orbit exists in highly prolate, triaxial potentials.

Subject headings: black hole physics – celestial mechanics, stellar dynamics – galaxies: nuclei

1. Introduction

Evidence for the presence of central black holes (BH) of mass, $10^6 - 10^{9.5}\,M_\odot$, appears strong for about a dozen galaxies (c.f. Kormendy and Richstone 1995). The masses of these objects are consistent with the mass in BHs needed to produce the observed energy in light from quasars (Soltan 1982, Chokshi and Turner 1992). Recent studies suggest that the dynamical influence of the BH extends to well outside the nuclear regions of its host galaxy, if the orbits of stars carry them close to the center (c.f. Merritt 1998 for a review). In particular, dynamical phenomena in the central regions are strongly influenced by the BH. Stars move in the combined gravitational potentials of the BH, and the surrounding mass of stars and gas (for brevity, these will be referred to as the "cluster"). The radius of influence of the BH (r_h) may be defined as radius of the sphere within which the mass of the surrounding stars and gas is less that of the BH. Within r_h, the potential of the BH dominates the dynamics, and the potential of the cluster may be considered to be a small perturbation. Sridhar and Touma (1999; hereafter referred to as ST99) studied stellar dynamics within r_h, and arrived at the following conclusions:

(i) Stellar orbits may be thought of as Keplerian ellipses that deform and precess over times that are longer than orbital times by a factor (M/M_c), where M_c is the mass of the cluster enclosed by the orbit. Well within r_h, $M/M_c \gg 1$.

(ii) The slow dynamics of precessional motions may be understood by *averaging* over the Keplerian orbital periods of stars, which are the shortest time scales in the problem.

(iii) Averaging gives rise to a secular integral of motion, $I \simeq \sqrt{GMa}$, where a is the semi–major axis of the orbit. Thus the BH enforces some degree of regularity in the structure of orbits that lie within r_h.

(iv) A stellar orbit in a time–independent cluster conserves two integrals of motion. These are the energy, which is an exact invariant, and the semi–major axis, which is secularly conserved.

(v) Thus clusters which may be modelled as razor–thin disks, or as three dimensional, axisymmetric objects, give rise to averaged dynamics that is integrable.

(vi) Non–axisymmetric, razor–thin disks, with power law surface density profiles have averaged dynamics, whose qualitative features are independent of the steepness of the power law. This occurs because, within r_h, the Kepler potential of the BH is far steeper than any self–gravitational force due to the cluster.

Here we take up the thread, and consider orbits in three dimensional clusters, which is a far more complicated problem than the cases studied by ST99. We specifically wish to focus on the effects of three dimensionality, and triaxiality. Recalling from item (vi) above that the qualitative features of orbital structure (arrangement of lens and loop orbits) are insensitive to the steepness of the cusp, we wish to choose a cusp steepness that would yield the simplest expression for the averaged Hamiltonian for our three dimensional problem. For the razor–thin disks studied by

ST99, the averaged Hamiltonian turned out to be a hypergeometric function of the eccentricity, for a general value of the cusp steepness; on the other hand, the harmonic case yielded the simplest expressions, composed only of elementary functions. Therefore, in our present venture into three dimensions, we restrict attention to a family of triaxial, harmonic potentials, average over the fast orbital motion, to obtain an expression for the Hamiltonian governing slow dynamics. As equations (4) and (5) show, only elementary functions occur in this Hamiltonian, which governs nearly Keplerian, three dimensional dynamics. The phase space of the averaged dynamics is four dimensional, hence the dynamics is well suited to exploration through Poincaré surfaces of section. Because of all these favourable features we consider the Hamiltonian of equations (4) and (5) as the "canonical" Hamiltonian governing three dimensional dynamics within the radius of influence. However, these nice features may be invalid when the orbital radius becomes comparable to r_h; in particular, the discrepancy between true dynamics, and averaged dynamics may be greater in three dimensions.

In § 2, we provide a quick introduction to action–angle variables for the Kepler problem, and averaging over the fast orbital frequency. We then study the orbital structure as a function of the energy (after subtracting out the Keplerian contribution). Averaging over the Keplerian motion, promotes the semi–major axis as a conserved quantity. For scale–free potentials, such as the harmonic potential, the orbital structure is similar at all radii for which the averaging procedure is valid; this motivates the scalings adopted later. Orbits that reinforces the shape of the generating potential, demands special attention. Such orbital families play a crucial role in the construction of self–consistent stellar dynamical models (e.g. Schwarzschild 1979, de Zeeuw 1996, Merritt 1999). Thus we also study the real space structure of orbits, when they appear worthy of mention. Averaged dynamics for oblate and prolate axisymmetric cases is discussed in § 3. We numerically integrate the equations of motion, and take Poincare sections. In § 4, we discuss the global orbital structure for the triaxial case, when departures from spherical symmetry are small (small oblateness or prolateness, but quite large triaxiality). The results are interpreted through secular perturbation theory.

The reader who is interested in getting a quick glimpse of the real–space structure of those orbits that reinforce triaxiality, as well as oblateness/prolateness of the potential, is advised to consult the list of relevant figures and comments provided at the end of the discussion in § 5.

2. Formulation of orbit–averaged dynamics

Let us locate the BH, of mass M, at the origin (this is a valid assumption, so along as the center of mass of the surrounding cluster does not vary with time). We introduce action–angle variables, appropriate to the Kepler problem, that allow us to conveniently carry out orbit–averaging. These are the Delaunay variables (c.f. Plummer 1960, Goldstein 1980). $I = \sqrt{GMa}$, L, and L_z are the actions, where L and L_z are the magnitude and z–component, respectively, of the angular momentum. We denote the conjugate angles by w, g and h, respectively. w is the orbital phase

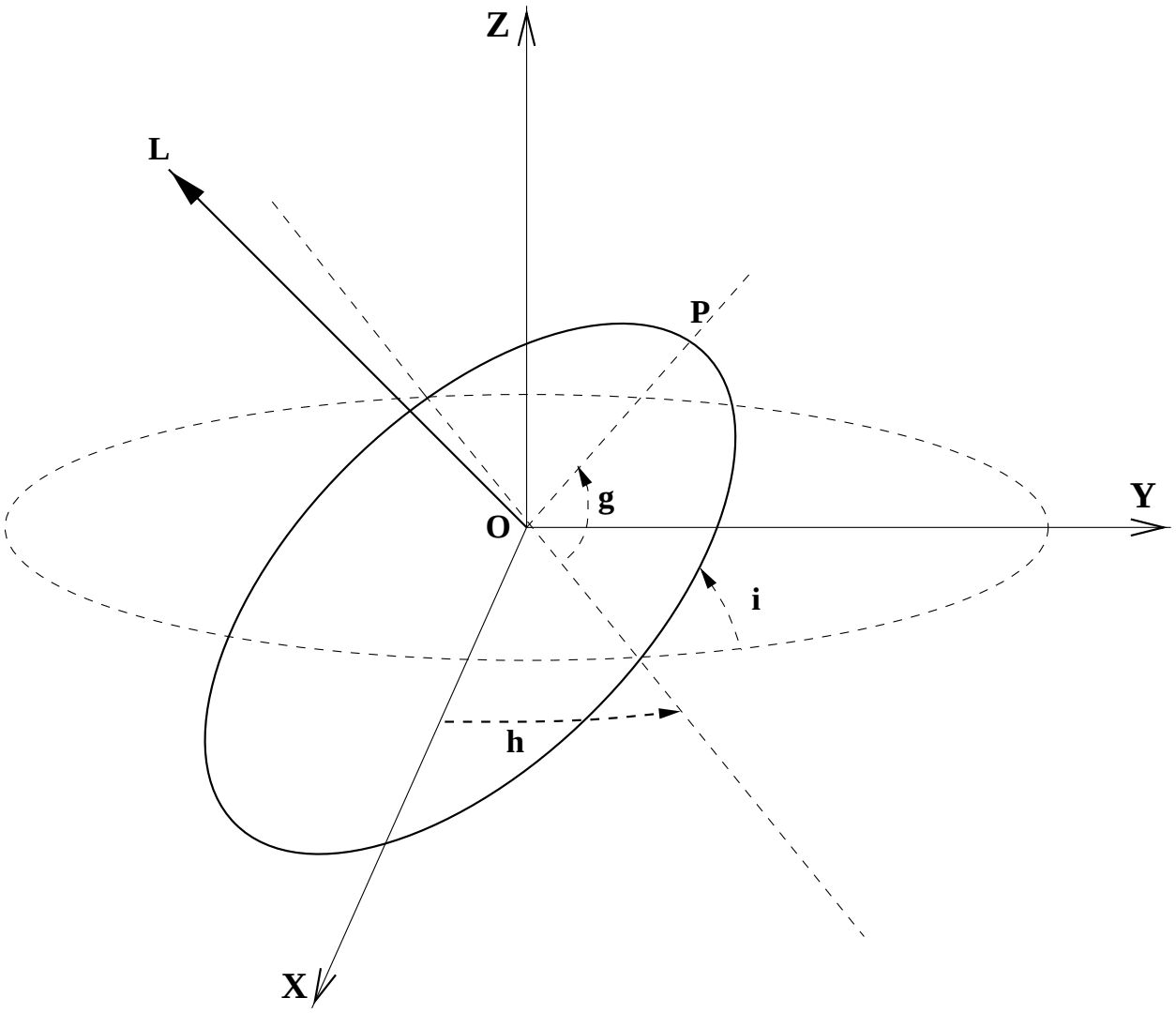

Fig. 1.— Orbital elements of the Kepler problem (Delaunay variables): the orbit is represented by the ellipse, drawn in bold line. **P** marks the pericenter. The figure shows only the four variables of precessional dynamics. The other two refer to the semi–major axis of the ellipse, and orbital phase.

("mean anomaly") which varies from 0 at pericenter to 2π after one orbit. g is the angle to the pericenter, measured from the ascending node, and h is the longitude of the ascending node (see Figure 1). For the Kepler problem, the only Delaunay variable that is time dependent is w: $w(t) = w_0 + (G^2M^2/I^3)\,t$.

Let $\Phi(x, y, z)$ be the perturbing gravitational potential of the cluster. To average Φ over the orbital phase, it is convenient to express the spatial coordinates in terms of the Delaunay variables (c.f. Goldstein 1985):

$$\begin{pmatrix} x \\ y \\ z \end{pmatrix} = \begin{pmatrix} C_gC_h - C_iS_hS_g & -S_gC_h - C_iS_hC_g & S_iS_h \\ C_gS_h + C_iC_hS_g & -S_gS_h + C_iC_hC_g & -S_iC_h \\ S_iS_g & S_iC_g & C_i \end{pmatrix} \begin{pmatrix} a(C_\eta - e) \\ a\sqrt{1-e^2}\,S_\eta \\ 0 \end{pmatrix} \tag{1}$$

where S and C are shorthand for sine and cosine of the angles given as subscript. i is the angle of inclination determined by $\cos i = L_z/L$, and $e = \sqrt{1 - L^2/I^2}$ is the eccentricity; as before, a is the semi–major axis. η is the eccentric anomaly, related to the orbital phase through $w = \eta - e\sin\eta$. Having substituted the expressions for (x, y, z), given in equation (1), in $\Phi(x, y, z)$, averaging is conveniently carried out by integrating over η:

$$\overline{\Phi} = \frac{1}{2\pi}\oint d\eta(1 - e\cos\eta)\,\Phi\,. \tag{2}$$

This orbit–averaged potential, $\overline{\Phi}$, plays the role of the Hamiltonian for slow, precessional dynamics (see ST99). Superimposed on the slow time variation of averaged dynamics are fast oscillations (with frequency of order $\sqrt{GM/a^3}$), whose fractional amplitudes are of order $\varepsilon \sim a\,(\Phi - \overline{\Phi})/GM$. Henceforth we assume that $\varepsilon \ll 1$, and ignore these fast oscillations. Note that, for fixed a, ε is larger for more eccentric orbits, because these sample a larger spatial variation of Φ. Because $\overline{\Phi}$ is independent of w, the conjugate variable, I, is secularly (i.e. on the average) conserved.

For investigation of orbital structure, we consider a family of triaxial, perturbing potentials of the form

$$\Phi(x, y, z) = \frac{\Phi_0}{r_0^2}\left(x^2 + \frac{y^2}{b_\varphi^2} + \frac{z^2}{c_\varphi^2}\right)\,, \tag{3}$$

Physically, this gravitational potential may be assumed to arise from a homogeneous, triaxial cluster whose center coincides with the location of the BH. The shape parameters of the potential (viz. b_φ and c_φ) are related to those of the density (say, b_ϱ and c_ϱ) and can be found in the literature (c.f. Chandrasekhar 1969, Binney and Tremaine 1987). The case when the potential is axisymmetric may be studied by setting $b_\varphi = 1$; oblateness, or prolateness is achieved by choosing c_φ to be less than, or greater than unity, respectively. More realistic, inhomogeneous mass distributions could be considered, but at the expense of considerably greater algebraic complexity.

Let $\mu = (\Phi_0 a^2/Ir_0^2)$ be a measure of the precession frequency for orbits with semi–major axis a. As in ST99 , it proves to be convenient to define a dimensionless time $\tau = \mu t$, Hamiltonian

$H = (\overline{\Phi}/\mu I)$, and angular momenta $\ell = L/I$ and $\ell_z = L_z/I$. Note that $0 \leq \ell \leq 1$, and $-1 \leq \ell_z \leq 1$. Averaging the potential of equation (3) over orbital phase, we obtain the dimensionless Hamiltonian

$$H(\ell, \ell_z, g, h) = \frac{1}{2}(5 - 3\ell^2) \; + \; \epsilon_c H_c(\ell, \ell_z, g) \; + \; \epsilon_b H_b(\ell, \ell_z, g, h)\,, \tag{4}$$

where

$$\begin{aligned} H_c(\ell, \ell_z, g) &= \frac{1}{4}\left(1 - \frac{\ell_z^2}{\ell^2}\right)\left(5 - 3\ell^2 - 5(1-\ell^2)\,C_{2g}\right)\,, \\ H_b(\ell, \ell_z, g, h) &= \left(\frac{5}{2} - 2\ell^2\right)\left(C_g S_h + \frac{\ell_z}{\ell} C_h S_g\right)^2 + \frac{\ell^2}{2}\left(-S_g S_h + \frac{\ell_z}{\ell} C_h C_g\right)^2\,, \end{aligned} \tag{5}$$

and $\epsilon_b = (b_\varphi^{-2} - 1)$, $\epsilon_c = (c_\varphi^{-2} - 1)$. This is the model two degree–of–freedom Hamiltonian that will be studied in the rest of this paper. The equations of motion are,

$$\dot{\ell} = -\frac{\partial H}{\partial g}\,, \quad \dot{g} = \frac{\partial H}{\partial \ell}\,; \qquad \dot{\ell_z} = -\frac{\partial H}{\partial h}\,, \quad \dot{h} = \frac{\partial H}{\partial \ell_z}\,, \tag{6}$$

where the over–dots refer to $(d/d\tau)$. We integrate these equations numerically using a fourth–order, adaptive step–size, Runge–Kutta scheme, and take surfaces of section at constant values of either of the angles g, or h. Thus we follow the the deformations of Keplerian ellipses of fixed semi–major axes, over time scales much longer than the orbital periods. This technique will, in principle, reveal all of the phase space structure of the orbits. We will also supplement the numerical calculations with analytical estimates, wherever necessary. Note that such an assault on orbits in triaxial potentials would have been impossible, without the presence of the extra integral of motion that averaging promotes.

The Hamiltonian, given in equations (4) and (5), is a constant of motion. The orbital structure shows strong dependence on the value of this quantity, and henceforth we will refer to it as the energy (E). Since, for the averaged dynamics, Kepler energy is constant, this refers refers to the average value of Φ over the orbit in question. The simplest case is that of spherical symmetry, when $\epsilon_b = \epsilon_c = 0$. Then $H = (5 - 3\ell^2)/2$, so that $\dot{\ell} = \dot{\ell_z} = \dot{h} = 0$, and $\dot{g} = -3\ell$: the Keplerian ellipses precess rigidly, at a constant rate in a retrograde sense, maintaining an invariant orbital plane.

3. Orbits in the axisymmetric case

When $b_\varphi = 1$, the potential of equation (3) is axisymmetric about the z–axis. Hence L_z is conserved even for the unaveraged dynamics. For slow dynamics, this implies that ℓ_z is an integral of motion, and we are left with a one degree–of–freedom system, whose dynamics is obviously

integrable. Setting $\epsilon_b = 0$, from equations (4) and (5), we obtain the following expression for the axisymmetric Hamiltonian,

$$H(\ell, g; \ell_z) = \frac{1}{2}(5 - 3\ell^2) \; + \; \frac{\epsilon_c}{4}\left(1 - \frac{\ell_z^2}{\ell^2}\right)\left(5 - 3\ell^2 - 5(1-\ell^2)\, C_{2g}\right) . \tag{7}$$

where ℓ_z is now regarded as a constant parameter. Note that ϵ_c is positive for oblate configurations, and negative for the prolate ones. The nodal precession rate given by

$$\dot{h} = \frac{\partial H}{\partial \ell_z} = -\frac{1}{2}\epsilon_c \frac{\ell_z}{\ell^2}\left[10\, S_g^2\,(1-\ell^2) + 2\ell^2\right] , \tag{8}$$

shows that the sign of $\dot{h}$ is opposite to that of the product, $\epsilon_c \ell_z$; hence nodal precession is prograde (retrograde) for prolate (oblate) potentials.

To obtain a global picture of the dynamics, it is instructive to plot an $\ell - g$ (Poincaré) surface of section taken at some fixed value of h; Figures 2a and 2b show two such sections for oblate ($c_\varphi < 1$) and prolate ($c_\varphi > 1$) potentials, respectively.

From these figures, it may be seen that the dynamics is organised around the elliptic fixed points, located at $g = \pi/2$ and $3\pi/2$. These are special orbits for which ℓ and g are constant in time, whereas h precesses steadily. Using the Hamiltonian of equation (7) in equations (6), it is straightforward to verify that these fixed point orbits (FPOs) are described by,

$$\ell^4 = \frac{5\epsilon_c \ell_z^2}{3 + 4\epsilon_c} , \qquad g = \pi/2 \;\; \text{or} \;\; 3\pi/2 , \qquad \dot{h} = 4\epsilon_c \ell_z - 5\epsilon_c \sqrt{\frac{3+4\epsilon_c}{5\epsilon_c}} . \tag{9}$$

Before we proceed to examine the dynamics in more detail, let us pause to consider some implications of equations (9) for FPOs (it is useful to recall that $0 \le \ell \le 1$, $-1 \le \ell_z \le 1$, and $\cos i = \ell_z/\ell$).

1. One end of the FPO sequence is set by $\ell_z = 0$, which is the z axial orbit (unless $3 + 4\epsilon_c = 0$, which is the case $c_\varphi = 2$).

2. Because $\ell^2 \propto \cos^2 i$, the orbits become rounder as their inclination decreases (i.e. as the orbital plane approaches the equator).

3. The other end of the FPO sequence is reached when either $i = 0$, or $\ell = 1$, whichever occurs first. This depends on whether $5\epsilon_c/(3 + 4\epsilon_c)$ is less than, or greater than unity (equivalently, when c_φ is greater than, or less than $1/2$). There is an additional requirement that $5\epsilon_c/(3 + 4\epsilon_c) \ge 0$, which implies that no FPOs of the kind allowed by equation (9) exist, for prolate potentials which have $1 < c_\varphi < 2$.

4. *Oblate:* $0 < c_\varphi < 1/2$: $\ell = 1$ is reached before $i = 0$, so there are no equatorial FPOs.

5. *Oblate:* $1/2 < c_\varphi < 1$: $i = 0$ is reached before $\ell = 1$. When $c_\varphi = 1/2$, equation (9) implies that $ell^2 = \cos^2 i$ for the FPO; thus both $i = 0$ and $\ell = 1$ are reached simultaneously.

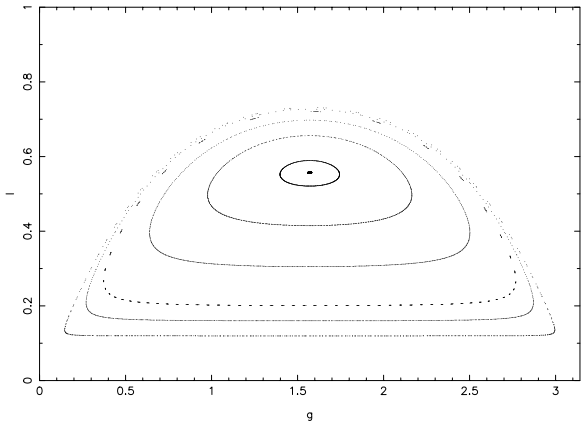

Fig. 2a. $\ell - g$ surface–of–section for oblate axisymmetric potential. $c_\varphi = 0.8$ and energy $E = 2.48$

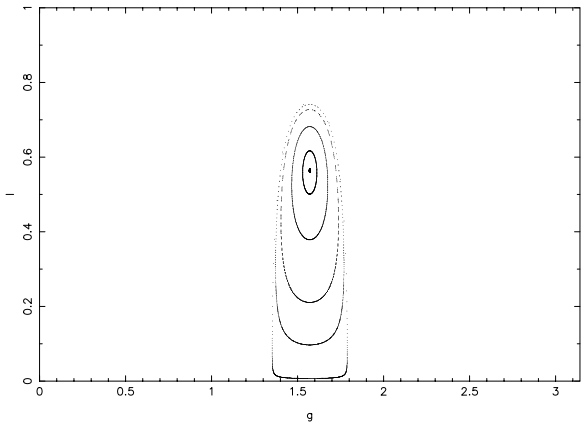

Fig. 2b. $\ell - g$ surface–of–section for prolate axisymmetric potential. $c_\varphi = 2.5$ and energy $E = 0.5$

6. *Prolate:* $c_\varphi > 2$: $\ell = 1$ is reached before $i = 0$, so there are no equatorial FPOs.

The Poincaré section may also be regarded from a different perspective. For the completely integrable dynamics of the axisymmetric problem, one may invert equation (7), to express ℓ_z as a function of ℓ, g and H,

$$\ell_z = \pm\,\ell\left(1 - \frac{1}{\epsilon_c}\,\frac{6\ell^2 + 4H - 10}{\ell^2(5C_{2g} - 3) + 5(1 - C_{2g})}\right)^{1/2} . \tag{10}$$

We may now regard H as a constant parameter, with the $\ell - g$ dynamics controlled by the Hamiltonian equal to $(-\ell_z)$, and "time" measured by h. Figures 2a and 2b may be reproduced by plotting the isocontours of ℓ_z in the $\ell - g$ plane. It is straightforward to verify the stability of the orbits of equation (9) by Taylor expanding ℓ_z about the fixed point values of ℓ and g. The FPOs parent a family of orbits for which both ℓ and g librate periodically, and h precesses non–uniformly

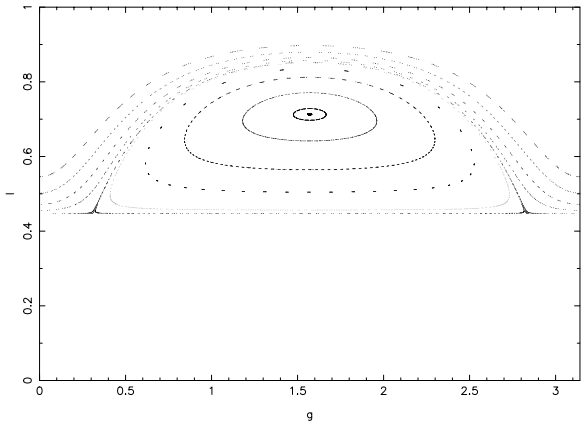

Fig. 2c. $\ell - g$ surface–of–section for oblate axisymmetric potential. $c_\varphi = 0.7$ and energy $E = 2.2$

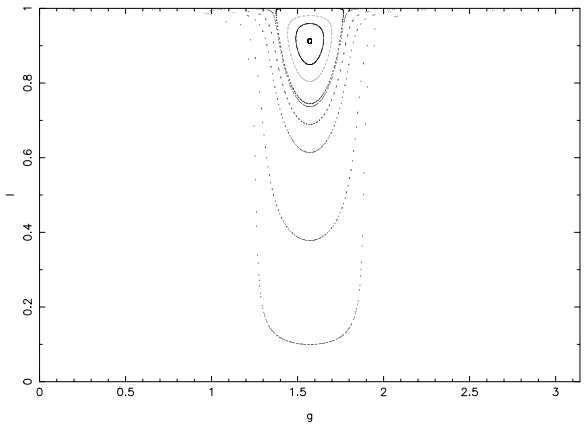

Fig. 2d. $\ell - g$ surface–of–section for prolate axisymmetric potential. $c_\varphi = 2.5$ and energy $E = 0.6$

in time. In real space, these orbits fill ("hollowed–out") conical regions whose axes coincide with the z–axis. The phase flows in the $\ell - g$ plane are structurally similar to those of a pendulum. Hence there are also other orbits for which g circulates, and these are distinguished from the former by a separatrix. Figures 2c and 2d show two representative sections of such orbits.

For prolate potentials with $1 < c_\varphi < 2$, the dynamics is quite different, as is revealed by the surface of section, shown in Figure 2e; g circulates for all orbits. This difference in behaviour is connected with the stability of the z–axis orbit. Let us test the z–axis orbit for stability to eccentricity variations which, however, maintain $\ell_z = 0$. We Taylor expand the right side of equation (7) about $\ell = 0$, and $g = \pi/2$. Setting $g = \pi/2 + \delta g$, we obtain

$$\frac{5}{2}(1 + \epsilon_c) - H = (\frac{3}{2} + 2\epsilon_c)\ell^2 + \frac{5}{2}\epsilon_c\,(\delta g)^2\,. \tag{11}$$

The energy of the z–axis orbit is $H = 5(1 + \epsilon_c)/2$, which is the maximum allowed energy in

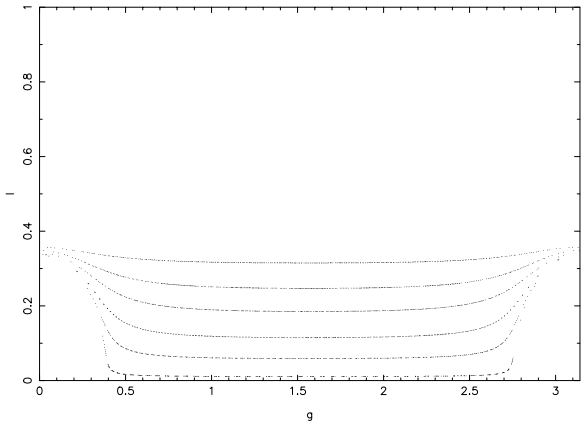

Fig. 2e. $\ell - g$ surface–of–section for prolate axisymmetric potential. $c_\varphi = 1.5$ and energy $E = 2.3$

the oblate case. Therefore, the left side is always non negative, as are the coefficients of ℓ^2 and $(\delta g)^2$; thus the z–axis orbit is always stable. For the prolate case, the energy of the z–axis orbit, $H = 5(1 + \epsilon_c)/2$, is the minimum allowed energy. Hence the left side is always non positive. The coefficient of $(\delta g)^2$ is negative, so the issue of stability depends on the sign of the coefficient of ℓ^2. It is clear that the z–axis orbit is stable for $\epsilon_c < -3/4$, and unstable when $-3/4 < \epsilon_c < 0$.

4. Orbits in the triaxial case.

The shape of the potential is given by two axes ratios, b_φ and c_φ. The definition of the Delaunay variables gives a privileged status to the z–axis, so we let this be the axis of symmetry for the study of orbits in the axisymmetric case. In particular, we set $b_\varphi = 1$, and chose $c_\varphi < 1$ and $c_\varphi > 1$ for oblate and prolate cases respectively. Whereas this is the most convenient choice for the dynamics, it implies that the ordering of the lengths of the x, y and z axes are different in the oblate and prolate cases. This feature carries over to triaxial configurations as well. Hence we allow b_φ and c_φ to take any positive value, and define the "triaxiality" to be $T = (a_1^2 - a_2^2)/(a_1^2 - a_3^2)$, where (a_1, a_2, a_3) are equal to the set $(1, b_\varphi, c_\varphi)$, after the latter has been rearranged (if necessary) in descending order of magnitudes. With this convention, for axisymmetric configurations, $T = 0$ for the oblate case, and $T = 1$ for the prolate case.

The equations of motion (eqn. 6), resulting from the Hamiltonian of equations (4) and (5), are

$$\dot{\ell} = \epsilon_c \left[\frac{5}{2}\left(1 - \frac{\ell_z^2}{\ell^2}\right)(1 - \ell^2) S_{2g}\right] - 5\epsilon_b \left[(1 - \ell^2)(C_g S_h + \frac{\ell_z}{\ell} C_h S_g)(-S_g S_h + \frac{\ell_z}{\ell} C_h C_g)\right] ,$$

$$\dot{\ell_z} = -\epsilon_b \left[(5 - 4\ell^2)(C_g S_h + \frac{\ell_z}{\ell} C_h S_g)(C_g C_h - \frac{\ell_z}{\ell} S_h S_g)\right]$$

$$+\epsilon_b \left[\ell^2(-S_g S_h + \frac{\ell_z}{\ell} C_h C_g)(S_g C_h + \frac{\ell_z}{\ell} S_h C_g) \right] ,$$

$$\begin{aligned}
\dot{g} &= -3\ell + \frac{1}{2}\epsilon_c \left[\frac{\ell_z^2}{\ell^3}(5 - 3\ell^2 - 5(1-\ell^2)C_{2g}) + \ell(1 - \frac{\ell_z^2}{\ell^2})(5C_{2g} - 3) \right] \\
&\quad -\epsilon_b \left[(C_g S_h + \frac{\ell_z}{\ell} C_h S_g)(4\ell C_g S_h + 5\frac{\ell_z}{\ell^2} C_h S_g) + \ell S_g S_h(-S_g S_h + \frac{\ell_z}{\ell} C_h C_g) \right] ,
\end{aligned}$$

$$\begin{aligned}
\dot{h} &= -\frac{1}{2}\epsilon_c \frac{\ell_z}{\ell^2}(5 - 3\ell^2 - 5(1-\ell^2)C_{2g}) \\
&\quad +\epsilon_b \left[(5 - 4\ell^2)\frac{1}{\ell} C_h S_g(C_g S_h + \frac{\ell_z}{\ell} C_h S_g) + \ell C_h C_g(-S_g S_h + \frac{\ell_z}{\ell} C_h C_g) \right] . \qquad (12)
\end{aligned}$$

We integrate these numerically, and take Poincaré sections by strobing in either of the angles g, or h. In this paper, we restrict our study to triaxial configurations that are close to spherical; thus b_φ and c_φ are close to unity (equivalently, ϵ_b and ϵ_c are close to zero). This allows us to use perturbation theory to understand the results of our numerical computations.

As in the axisymmetric case we study the orbital structure as a function of the (constant value of) Hamiltonian, which we refer to as the "energy". Recall that the Hamiltonian is equal to the (scaled) potential of the cluster. The scaling simply means that we have chosen to explore the dynamics of nearly Keplerian orbits with unit semi–major axis. Hence the lowest energy orbits are circular, and the highest energy orbits very eccentric. Below we explore both oblate and prolate triaxial cases. As representative cases, we consider (b_φ, c_φ) equal to $(0.99, 0.96)$ and $(0.99, 1.04)$, for the oblate and prolate triaxial potential. It may be verified that the triaxiality is quite large, namely $T \simeq 0.254$, and 0.804, respectively.

4.1. Low energy orbits; $\ell \lesssim O(1)$

Recall that ℓ_z was a constant of motion in the axisymmetric case; a Poincaré section, strobed in g would have given horizontal rows of dots in the $\ell_z - h$ plane. Hence this surface of section is very useful in revealing the effects of triaxiality, as may be seen in Figures 3a and 3b, which show a pendulum-like dynamics of the $\ell_z - h$ motions. The figures do not, of course, reveal that the periapse angle, g, always circulates (but this has been verified by plotting $\ell - g$ sections, and by following the time evolution of g). A glance at the equations of motion (12) shows that $|\dot{g}| \sim O(1)$, whereas $|\dot{h}| \sim O(\epsilon_c) \ll |\dot{g}|$. Therefore, it is useful to imagine the motion of the Keplerian ellipses on two well–seperated timescales. At nearly constant values of h and i (i.e. on a nearly fixed orbital plane), the precessing ellipse fills a circular annulus. On a longer timescale, the orbital plane itself either circulates or librates in h, while oscillating in inclination. As in the axisymmetric case, oblate triaxial configurations give rise to retrograde precession of h while prograde precession results in the prolate case. In Figure 3a, the librating and circulating orbits are long–axis and short–axis tubes, respectively; in Figure 3b, the roles are reversed. These orbits are also found in

more general triaxial galactic potentials with constant density cores. Their persistence in the case when a black hole is present may be understood qualitatively by noting that these tube orbits are round ($\ell \lesssim O(1)$), so they are not destabilized by the black hole (note that the lower ℓ orbits of § 4.2 are completely different).

The dynamics can be understood by averaging over the fast angle g. Equations (4) and (5), when averaged over g give

$$\langle H \rangle_g = \frac{1}{2}(5 - 3\ell^2) \left[1 \; + \; \frac{\epsilon_c}{2} \left(1 - \frac{\ell_z^2}{\ell^2} \right) \; + \; \frac{\epsilon_b}{2} \left(S_h^2 \; + \; \frac{\ell_z^2}{\ell^2} \, C_h^2 \right) \right] , \tag{13}$$

for the Hamiltonian describing the slower dynamics of ℓ_z and h; it is straightforward to verify that the isocontours of this Hamiltonian reproduce the surfaces of sections shown in Figures 3a and 3b. In this approximation, ℓ emerges as a secular invariant (i.e. no secular variation in eccentricity), and the g–averaged dynamics reduces to a one degree of freedom system in the variables, ℓ_z and h.[1] The orbits corresponding to circulations of h (short and long axes tubes, for oblate and prolate cases, respectively) have larger $|\ell_z|$, so are more nearly *equatorial*. The orbit fills a region of space that is toroidal and non axisymmetric. The approximate axis of symmetry is along the z–axis, and the torus itself could be thought of as somewhat pinched along the intermediate axis (y for oblate and x for prolate).

The orbits for which h librates (and ℓ_z flips sign), have smaller values of $|\ell_z|$, so these are more nearly *polar* (long and short axes tubes, for oblate and prolate cases, respectively). Let us first consider the parent polar orbit with $\ell_z = 0$. For the oblate/prolate cases, the orbit lies in a plane perpendicular to the long/short axis. Within the plane, g circulates rapidly and nearly uniformly, while ℓ shows equally rapid, small amplitude oscillations; hence the orbit fills an elliptical annular region. Figure 4 shows projections of a polar orbit on the three principal planes for a prolate case. The orbit lies essentially in the plane of the long and the intermediate axes, so reinforces the shape of the potential to some extent.

4.2. High energy orbits: $\ell \sim O(\sqrt{\epsilon_c})$

High energy orbits are characterised by low angular momentum values, hence are all quite eccentric. In general, $\ell \sim O(\sqrt{|\epsilon_c|})$. This regime of energy admits a certain scaling, that allows us to parametrise the dynamics by the single quantity; $B = \epsilon_b/|\epsilon_c|$. Let us introduce the scaled variables,

$$l = \frac{\ell}{\sqrt{|\epsilon_c|}} , \qquad l_z = \frac{\ell_z}{\sqrt{|\epsilon_c|}} , \qquad K = \frac{1}{|\epsilon_c|} \left(H - \frac{5}{2} \right) , \qquad s = \sqrt{|\epsilon_c|} \, \tau , \tag{14}$$

[1] A more systematic approach to averaging over the fast angle uses first order perturbation theory, whose primary advantage over equation (13) is that the $O(\epsilon_c)$ oscillations in ℓ are well represented.

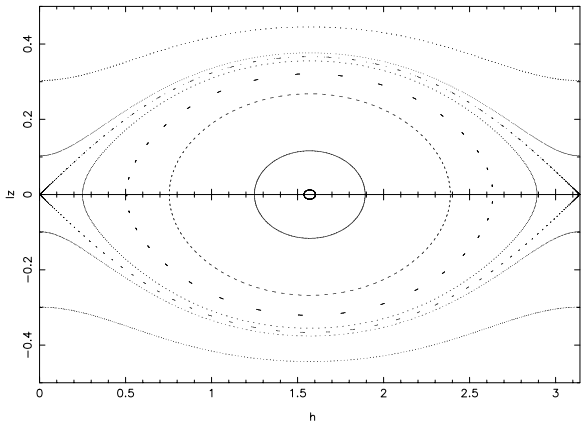

Fig. 3a. $\ell_z - h$ surface–of–section (strobed at $g = \pi/2$) for oblate triaxial potential. $b_\varphi = 0.99$, $c_\varphi = 0.96$ and energy $E = 1.8$

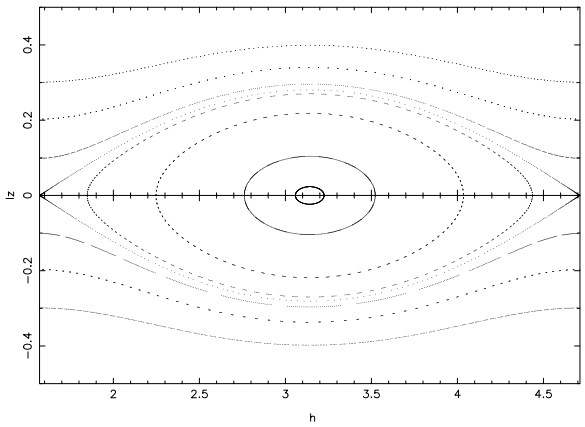

Fig. 3b. $\ell_z - h$ surface–of–section (strobed at $g = \pi/2$) for prolate triaxial potential. $b_\varphi = 0.99$, $c_\varphi = 1.04$ and energy $E = 1.8$

where (l, l_z) are conjugate to (g, h), and K and s are the new Hamiltonian and time, respectively, for this very slow dynamics of highly eccentric motions. Substituting the new variables in equations (4) and (5), we obtain

$$K = -\frac{3}{2}l^2 \; + \; sgn(\epsilon_c)\frac{5}{4}\left(1 - \frac{l_z^2}{l^2}\right)(1 - C_{2g}) \; + \; \frac{5B}{2}\left(C_g S_h + \frac{l_z}{l} S_g C_h\right)^2 \; + \; O(\epsilon_b, \epsilon_c)\,. \qquad (15)$$

where $sgn(\epsilon_c)$ is $\pm$, for ϵ_c positive/negative. Whereas the scaling is useful in restricting dependence to one parameter, B, the dynamics still concerns two coupled degrees of freedom, and no further reduction is, in general, possible. However, K is algebraically simpler to handle than H and we use it to understand the results of numerical integrations of the full equations of motion (eqns. 12). The dynamics of these highly eccentric orbits differs in the oblate and prolate triaxial potentials.

4.2.1. Oblate triaxial potential

Figures 5a and 5b are Poincaré sections, strobed in g and h respectively; it is important to note that the $\ell_z - h$ section is taken at $g = \pi/2$ (mod2π), but the precise value of the strobing in h, for the $\ell - g$ section is immaterial. Figure 5a is very similar to Figure 3a, with the notable addition of elliptic fixed points at $h = 0$ and π, located at non zero values of $|\ell_z|$. Moreover, Figure 5b shows them to be triaxial versions of the axisymmetric fixed points, discussed in § 3 (see Figure 2a). Recall that, in the axisymmetric case, the fixed point orbit corresponded to the steady rotation, about the z–axis, of an inclined, rigid Keplerian ellipse. The main effect of triaxiality is to introduce oscillations into quantities that were steady in the axisymmetric case. A question of interest is whether these oscillations change the shape of the orbit in a manner that reinforces the shape of the potential. Figure 6 shows the behaviour in time of g, h, i and e, where it may be seen that the librations of g (about $\pi/2$, or $3\pi/2$) occur at *twice* the frequency at which h precesses. Physically, this can be thought of as an $m = 2$ perturbation of an axisymmetric problem. Below we provide an analysis of this perturbation, and derive expressions the quantitative effects of triaxiality on various quantities of interest, such as the energy at which the FPO appears, the amplitudes of oscillation induced in ℓ, ℓ_z, and g.

Let us rewrite K (eqn. 15) as the sum of two terms, K_1 and K_2; K_1 contains terms that are independent of h, and K_2 consists of the remaining h dependent terms.

$$\begin{aligned} K &= K_1 + K_2 \,, \\ K_1 &= -\frac{3}{2}l^2 \;+\; \frac{5}{4}\left(1 - \frac{l_z^2}{l^2}\right)(1 - C_{2g}) \;+\; \frac{5B}{4}\left(C_g^2 + \frac{l_z^2}{l^2}S_g^2\right) \,, \\ K_2 &= \frac{5B}{4}\left(-C_g^2 C_{2h} + \frac{l_z^2}{l^2}S_g^2 C_{2h} + \frac{l_z}{l}S_{2g}S_{2h}\right) \,. \end{aligned} \tag{16}$$

K_1 may be viewed as an effective axisymmetric system that reduces to the actual axisymmetric case as $B \to 0$. Clearly, l_z is an integral of motion for this system, which we henceforth denote as l_{z_0}. The Hamiltonian K_1 admits elliptic fixed points at

$$g_0 = \frac{\pi}{2}\,, \frac{3\pi}{2}\,, \qquad\qquad l_0 = \left[\frac{5}{3}\left(1 - \frac{B}{2}\right)l_{z_0}^2\right]^{1/4} \,, \tag{17}$$

for which the nodal angle h circulates uniformly in the retrograde sense at a frequency, $\dot{h_0} = -\sqrt{15(1 - B/2)}$, which is independent of the value of l_{z_0}. When B equals zero, this expression coincides with the $\dot{h_0}$ of eqn (9), upto $O(\epsilon_c)$. The fixed point value of the energy, K_{1_0} is fixed by the value of the parameter l_{z_0}. The minimum value of energy at which such a fixed point is admitted is then obtained by sustituting the above fixed point values of l and g in the Hamiltonian K_1, and also noting that the maximum value l_z can take is equal to l. Thus,

$$K_{1_{min}} = \frac{5}{2}(B - 1)\,, \tag{18}$$

from which we obtain (using equation (14)),

$$E_0 = \frac{5}{2} + |\epsilon_c| K_{1_{min}} \;=\; \frac{5}{2}(1 - \epsilon_c + \epsilon_b). \tag{19}$$

The Hamiltonian K_2 acts as a perturbation on this effective axisymmetric system. Below we present a first order analysis of the perturbed fixed point orbit. To this end, let (l_1, g_1, l_{z_1}, h_1) be the perturbations to the fixed point values of the effective axisymmetric system, (l_0, g_0, l_{z_0}, h_0). Recalling that (l_0, g_0, l_{z_0}) are constant in time, and $h_0 = -\sqrt{15(1 - B/2)}s$, we note that the observed oscillations in the values of the dynamical variables (see Figure 6) will be described by (l_1, l_{z_1}, g_1, h_1). Hamilton's equations of motion, given by,

$$\begin{aligned}
\frac{dl_1}{ds} &= -\,l_1 \left(\frac{\partial^2 K_1}{\partial l \partial g}\right)_0 - \, l_{z_1} \left(\frac{\partial^2 K_1}{\partial l_z \partial g}\right)_0 - \, g_1 \left(\frac{\partial^2 K_1}{\partial g^2}\right)_0 - \left(\frac{\partial K_2}{\partial g}\right)_0 , \\
\frac{dg_1}{ds} &= l_1 \left(\frac{\partial^2 K_1}{\partial l^2}\right)_0 + \, l_{z_1} \left(\frac{\partial^2 K_1}{\partial l_z \partial l}\right)_0 + \, g_1 \left(\frac{\partial^2 K_1}{\partial g \partial l}\right)_0 + \left(\frac{\partial K_2}{\partial l}\right)_0 , \\
\frac{dl_{z_1}}{ds} &= -\left(\frac{\partial K_2}{\partial h}\right)_0 , \\
\frac{dh_1}{ds} &= l_1 \left(\frac{\partial^2 K_1}{\partial l \partial l_z}\right)_0 + \, l_{z_1} \left(\frac{\partial^2 K_1}{\partial {l_z}^2}\right)_0 + \, g_1 \left(\frac{\partial^2 K_1}{\partial g \partial l_z}\right)_0 + \left(\frac{\partial K_2}{\partial l_z}\right)_0 ,
\end{aligned} \tag{20}$$

admit the following solutions,

$$\begin{aligned}
l_1 &= \frac{1}{4}\left(\frac{5}{3}\right)^{3/4} B \left(1 - \frac{B}{2}\right)^{-1/4} l_{z_0}^{-1/2} \cos 2\omega_h s \,, \\
g_1 &= \frac{1}{2}\left(\frac{5}{3}\right)^{1/4} B \left(1 - \frac{B}{2}\right)^{-3/4} l_{z_0}^{-1/2} \sin 2\omega_h s \,, \\
l_{z_1} &= \frac{B}{4}\left(1 - \frac{B}{2}\right)^{-1} \cos 2\omega_h s \,, \\
h_1 &= -\frac{B}{4}\left(1 - \frac{B}{2}\right)^{-1/2} \left[\frac{1}{2} + \sqrt{\frac{5}{3}} l_{z_0}^{-1}\right] \sin 2\omega_h s \,, \\
h_0 &= \omega_h s \,,
\end{aligned} \tag{21}$$

where, $\omega_h = -\sqrt{15(1 - B/2)}$. Thus it is clear that the frequency of the small amplitude oscillations is twice that of the mean rotation of h. Moreover, l and l_z oscillate *in phase*, whereas the oscillations of g about its fixed point value and those of h about its mean rotation are *in phase*. Note that the amplitude of these oscillations decreases to zero as $B \to 0$, as expected for the axisymmetric case. Table 1 compares the predictions of our first–order theory with the results of numerical integrations of the exact equations of motion, for two different values of B. The smaller the value of B, the better is the match between the observed and predicted values.

Figure 7 shows the projections of one such FPO along the three symmetry planes defined by, the long and the intermediate axes (X–Y plane), the intermediate and the short axes (Y–Z plane), and the long and the short axes (X–Z plane). The orbit can be viewed as a highly elongated ellipse, rotating about the minor axis (here Z–axis) in a nonuniform manner. The orbit makes a nonzero inclination that exhibits a small libration about its mean value. Corresponding to these librations, is a deformation of the ellipse itself, resulting in periodic changes of its eccentricity. It is apparent from the figures that the orbit fills a conical region in space. The orbital extent is maximum along the long axis, and minimum along the short axis.

The orbit corresponding to the separatrix of Figure 5b, is shown in projection in Figure 8. This is seen to fill a rounder region of space than the fixed point orbit. It is interesting to note that both orbits (shown in Figure 7 and Figure 8) have shapes that appear to largely reinforce the triaxiality, as well as the oblateness of the potential.

Table 1: The observed and the predicted values of E_0, and the relative amplitudes of the fluctuations in ℓ, ℓ_z and g for the fixed point orbit in oblate triaxial potential. Note that smaller the value of B, better is the match in values.

	B	T	E_0	$(l_1/l_0)_{max}$	$(l_{z_1}/l_{z_0})_{max}$	$(g_1/g_0)_{max}$
	0.118	0.127				
Observed			2.334	0.548	0.031	0.059
Predicted			2.312	0.541	0.031	0.052
	0.239	0.254				
Observed			2.356	0.170	0.065	0.120
Predicted			2.331	0.110	0.067	0.110

4.2.2. Prolate triaxial potential

Figures 9a and 9b show Poincaré sections, strobed at $h = 0$ and $g = \pi/2$ respectively for a triaxial potential, whose prolateness is small (c_φ larger than, but close to unity). Both sections

show FPOs surrounded by islands of stability. Recall that prolate axisymmetric potentials, with $1 < c_\varphi < 2$ do not admit elliptic fixed points, for any value of the energy (compare Figure 9a with Figure 2e). Hence this fixed point is a purely triaxial phenomenon, which is conveniently described in the $\ell_z - h$ surface of section. Now compare Figure 9b with Figure 3b. Both the configurations have the same triaxiality, but different energies. Note that the stable fixed point at $\ell_z = 0$ in Figure 3b has changed its character to an unstable fixed point, as seen in Figure 9b. The latter figure also shows emergence of two stable fixed points, which were absent at low energies. It should be emphasised that these fixed points appear only above a certain minimum energy, E_0. The occurance of these fixed points can be explained by adhereing to an analogy with parametric resonance.

Consider the Hamiltonian K, given in equation (15)[2]. Expanding K about the fixed point $(l_z, h) = (0, 0)$, and keeping terms upto quadratic order in l_z and h, we write

$$\begin{aligned} K &= K_g + K_h, \\ K_g &= -\left(\frac{3}{2}l^2 + \frac{5}{4}(1 - C_{2g})\right), \\ K_h &= \left(\frac{5(1+B)}{4l^2}(1 - C_{2g})\right) l_z^2 + \left(\frac{5B(1+C_{2g})}{4}\right) h^2 + \left(\frac{5BS_{2g}}{2l}\right) l_z h\,. \end{aligned} \tag{22}$$

K_g and K_h may be viewed as the two coupled oscillators. K_h is quadratic in the small quantities, l_z and h, hence$|K_h| \ll |K_g|$, and we may make the approximation,

$$\dot{l} \simeq -\frac{\partial K_g}{\partial g}\,, \qquad\qquad \dot{g} \simeq \frac{\partial K_g}{\partial l}\,. \tag{23}$$

These equations are identical to those of a pendulum, and are readily solved. Of the two possible kinds of motion, libration and circulation, it is the latter that turns out to be relevant for our problem. We now regard l and g as given functions of time in K_h, and solve the following equations,

$$\dot{l_z} = -\frac{\partial K_h}{\partial h}\,, \qquad\qquad \dot{h} = \frac{\partial K_h}{\partial l_z}\,. \tag{24}$$

to obtain $l_z(t)$ and $h(t)$. Thus the dynamics has been reduced to a master–slave system, where the $\ell_z - h$ oscillations are driven by the $\ell - g$ motion. As the energy of the system is increased, the forcing frquency of the K_g pendulum changes, leading to a parametric instability in the $\ell_z - h$ system. This renders the $\ell_z - h$ fixed point hyperbolic, simultaneously giving birth to two new stable fixed points, as shown in Figure 9b. The separation between the new, stable, fixed points increases with energy. Below, we estimate E_0 by considerations appropriate to the onset of this parametric instability. We note that K_g is nearly constant, and eliminate l in favour of K_g and g. This is substituted in the expression for K_h in equation (23), to obtain

$$K_h = \left(-\frac{15}{2}\frac{(1 - C_{2g})(1+B)}{(4K_g + 5(1 - C_{2g}))}\right) l_z^2 + \left(\frac{5B(1+C_{2g})}{4}\right) h^2 + \left(\frac{5\sqrt{3}BS_{2g}}{\sqrt{-2(4K_g + 5(1 - C_{2g})}}\right) l_z h. \tag{25}$$

[2]This choice of the Hamiltonian already implies that one is looking at potentials with small $|\epsilon_c|$

Because the angle g circulates, we average the Hamiltonian, given in equation (25) over g, to obtain,

$$\langle K_h \rangle_g = \left(-\frac{3(1+B)}{2} \left(1 - \sqrt{\frac{2K_g}{5+2K_g}} \right) \right) l_z^2 + \frac{5B}{4} h^2 \,. \tag{26}$$

The cross term in $l_z - h$ has dropped out, leaving behind a simple harmonic oscillator, whose frequency of small oscillations is,

$$\omega_h = \sqrt{-\frac{15}{2} B(1+B) \left(1 - \sqrt{\frac{2K_g}{5+2K_g}} \right)} \,. \tag{27}$$

This should be compared with the frequency of circulation of the K_g pendulum,

$$\omega_g = \sqrt{-24 \left(K_g + \frac{5}{4} \right)}. \tag{28}$$

We expect parametric resonance when $\omega_g \simeq 2\omega_h$. Imposing this condition on equations (27) and (28), gives us an fifth order, algebraic equation for K_g, whose one real root gives us a prediction for the minimum energy, $E_0^{pre} = (5/2) + |\epsilon_c| K_g$, at which the $(\ell_z = 0, h = \pi)$ fixed point goes unstable, and bifurcates into two new elliptic fixed points. Table 2, given below, compares E_0^{pre}, with the minimum energy, E_0, obtained from numerical integrations of the full equations of motion.

Table 2: The observed and the predicted values of the minimum energy E_0 for the fixed point orbit for various prolate triaxial potentials. The superscripts *obs* and *pre* refer to the observed and the predicted values.

B	T	E_0^{obs}	E_0^{pre}
0.523	0.670	2.36	2.39
0.354	0.754	2.31	2.34
0.269	0.804	2.27	2.30

Figure 10 shows projections of one such FPO on the principal planes. The orbit reinforces the prolateness, as well as the triaxiality of the potential.

4.2.3. Triaxial potential, with large prolateness

When $c_\varphi > 2$, the prolate, axisymmetric potential admits a fixed point orbit, which survives the introduction of some triaxiality. Figure 11 is a Poincaré section strobed at $h = \pi/2$ for a prolate triaxial configuration with $c_\varphi = 2.5$ and $b_\varphi = 0.99$. This figure is very similar to Figure 2b. The projections onto the principal planes reveals that the orbit strongly reinforces both the triaxiality and the prolateness of the potential. Figure 12 shows real space projections of such a FPO.

5. Discussion

In the nuclear regions of galaxies, stars move in the combined gravitational fields of the central, supermassive black hole (BH), and the self–gravity of the cluster of stars. When the cluster is triaxial, the only integral of motion that orbits respect is the energy, and orbital structure is notoriously difficult to understand. We have applied the orbit–averaging method of ST99 to study stellar orbits that lie within the radius of influence of BH, where the gravitational potential of the cluster is a small perturbation to the Keplerian potential of the BH. Averaging over the orbital phase of the fast, nearly Keplerian motion promotes an additional integral of motion: for a time independent perturbation, this integral is the semi–major axis. Hence the problem reduces in dimension to the dynamics of the two precessional degrees of freedom. For this first effort at addressing the effect of triaxiality, we modeled the potential of the cluster by a triaxial, harmonic potential (the averaging method itself applies to general potentials); the rationale for this choice is discussed in some detail in the Introduction. We formulated the equations of motion using Delaunay variables (which are the action–angle variables of the Kepler problem), and integrated orbits numerically; appropriate Poincare sections provide global information on the dynamics.

The averaged dynamics of the axisymmetric case is completely integrable, and the orbital structure can be easily analysed. Both oblate and prolate axisymmetric potentials admit resonant orbits that parent families of their own. See §3 for a detailed listing of the properties of these orbits. Kozai (1962) discussed a similar problem in the context of the motion of asteroids perturbed by Jupiter. More recently, Holman, Touma and Tremaine (1997) have also considered the axisymmetric problem in the context of the dynamics of a planet orbiting the star, 16 Cyg B, being perturbed by the distant stellar companion, 16 Cyg A.[3]

In the triaxial case, the averaged dynamics admits two integrals of motions; the energy, which is exactly conserved, and the semi–major axis, which is secularly conserved. We undertook a systematic study of the nearly spherically symmetric case which, however, was quite highly

[3]In both cases, the perturber was modeled as a circular ring, and the tidal field was truncated at quadrupolar order, giving rise to an axisymmetric, harmonic potential of the form given in our equation (3), with $\Phi_0 < 0$, $b_\varphi = 1$, and $c_\varphi = 1/\sqrt{2}$.

triaxial. Chaos appeared to be, suppressed, and we identified appropriate effective third integrals in the several cases we studied. This could be a result of the reduction in degrees offered by averaging over the fast Keplerian motion. Averaging will be an increasingly invalid procedure as the size of the orbit approaches r_h; it will not surprise us if the three dimensional dynamics is significantly chaotic for these larger orbits.

Our study of the averaged dynamics of the triaxial case has turned up several resonant orbits, many of which appear to reinforce the triaxiality, as well as the oblateness/prolateness of the potential. Below we provide a brief travel guide.

1. *Polar orbits in prolate, triaxial potential* : Projections on principal planes given in Figure 4. Poincaré section in Figure 3b. Discussed in § 4.1. Orbit fills elliptical annulus in the plane of the intermediate and long axes.

2. *Resonant orbit in oblate triaxial potential* : Projections on principal planes given in Figure 7. Poincaré section in Figures 5a and 5b. Discussed in § 4.2.1. Orbit fills a hollow conical region, of elliptical cross section, whose axis is oriented along the short axis of the potential.

3. *Separatrix orbit in oblate triaxial potential* : Projections on principal planes given in Figure 8. Poincaré section in Figures 5b. Mentioned in § 4.2.1. Orbit fills a three dimensional box–like region, whose dimensions are compatible with the shape of the potential. Orbit spends a lot of time in the equatorial plane.

4. *Resonant orbit 1 in prolate triaxial potential* : Projections on principal planes given in Figure 10. Poincaré section in Figures 9a and 9b. Discussed in § 4.2.2. Orbit present only for small prolateness. Shaped like a butterfly.

5. *Resonant orbit 2 in prolate triaxial potential* : Projections on principal planes given in Figure 12. Poincaré section in Figures 11. Discussed in § 4.2.3. Orbit present only for large prolateness. Fills a hollow gourd–like region. Highly reinforces triaxiality. A promising candidate for constructing self–consistent models.

6. Acknowledgements

We thank an anonymous referee for laboring with a dense manuscript, and patiently criticising incomplete, sometimes incorrect, statements. NS thanks the Council of Scientific and Industrial Research, India, for financial support through grant 2–21/95(II)/E.U.II.

REFERENCES

Binney, J., & Tremaine, S., 1987, Galactic Dynamics, (Princeton University Press, Princeton)

Chandrasekhar, S., 1969, Ellipsoidal Figures of Equilibrium, (Dover, New York)

Chokshi, A., & Turner, E. L., 1992, MNRAS, 259, 421

de Zeeuw, P. T., 1996, Gravitational Physics, Proc. 36th Herstmonceux Conf., (Cambridge University Press)

Goldstein, H., 1980, Classical Mechanics, 2nd ed. (Reading: Addison-Wesley)

Holman, M., Touma, J., & Tremaine, S., 1997, Nature, 386, 254

Kormendy, J., & Richstone, D., 1995, ARAA 33, 581

Kozai, Y., 1962, AJ, 67, 591

Merritt, D., 1998, Comments on Astrophysics, 19

Merritt, D., 1999, PASP, 111, 129

Plummer, H. C., 1960, An Introductory Treatise on Dynamical Astronomy (Dover, New York)

Schwarzschild, M., 1979, ApJ, 232, 236

Soltan, A., 1982, MNRAS, 200, 115

Sridhar, S., & Touma, J., 1999, MNRAS, 303, 483

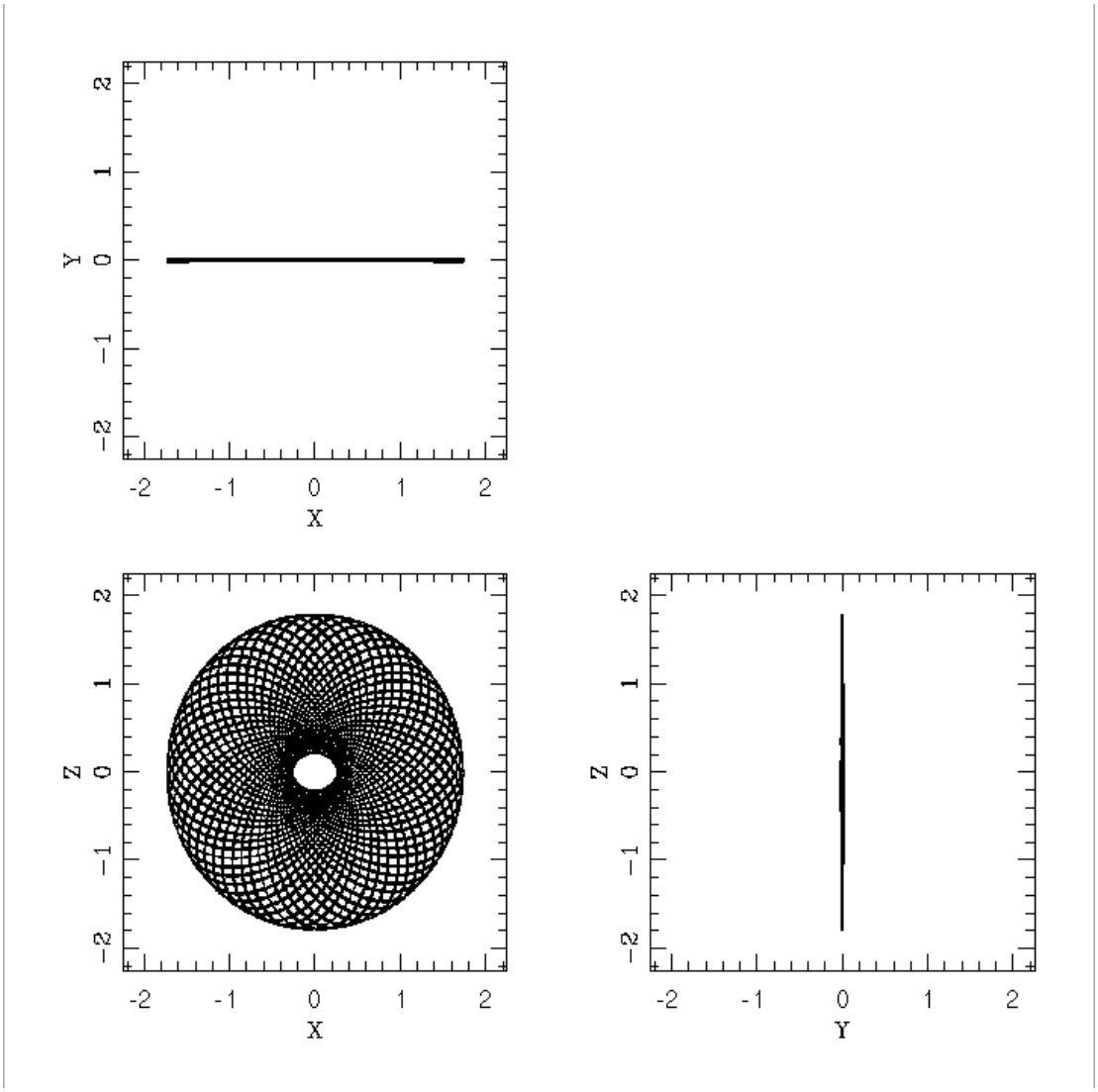

Fig. 4. Real space projections of a polar orbit in prolate triaxial potential. $b_\varphi = 0.99$, $c_\varphi = 1.04$ and energy $E = 1.8$

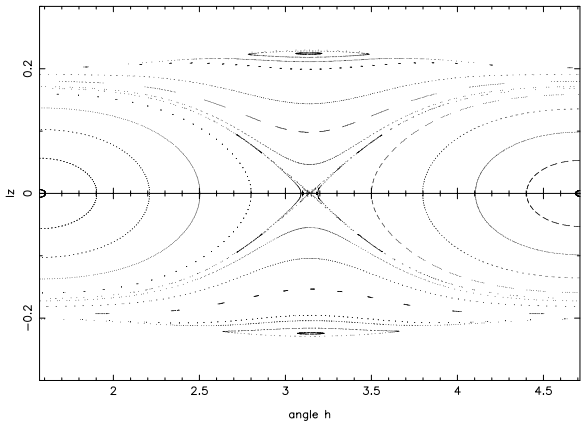

Fig. 5a. $\ell_z - h$ surface–of–section (strobed at $g = \pi/2$) for oblate triaxial potential. $b_\varphi = 0.99$, $c_\varphi = 0.96$ and energy $E = 2.48$

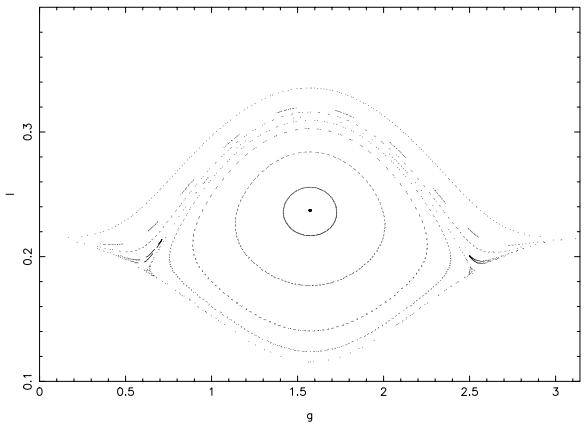

Fig. 5b. $\ell - g$ surface–of–section (strobed at $h = \pi/2$) for oblate triaxial potential. $b_\varphi = 0.99$, $c_\varphi = 0.96$ and energy $E = 2.48$

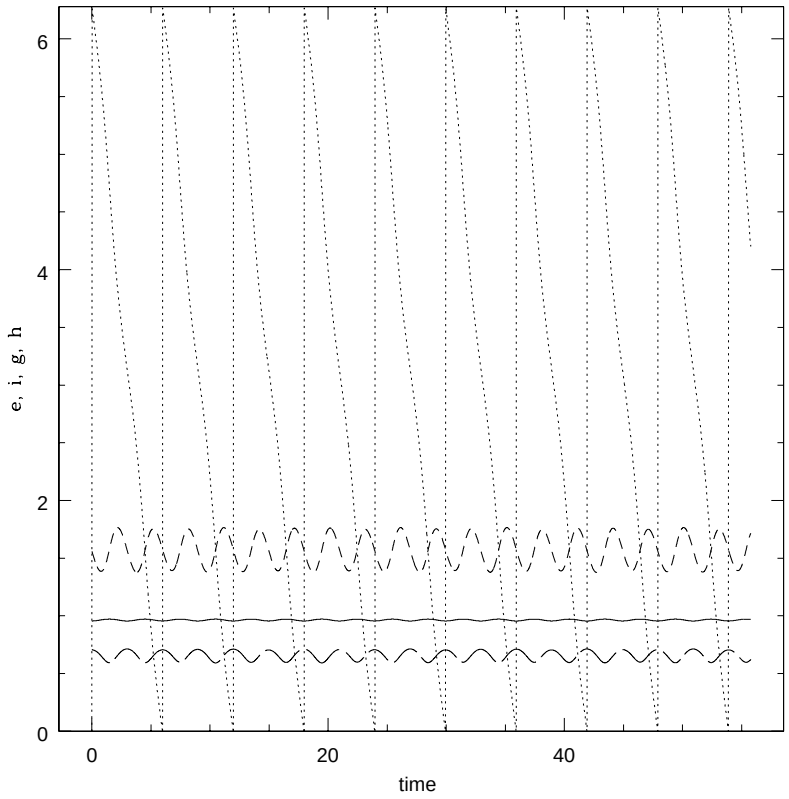

Fig. 6. Temporal behaviour of i, e, g, h for the $\ell - g$ fixed point orbit in oblate triaxial potential with $b_\varphi = 0.99, c_\varphi = 0.96,$ and $E = 2.48$. The long–dashed, solid, short–dashed, and the dotted curves, correspond to i, e, g, h, repsectively.

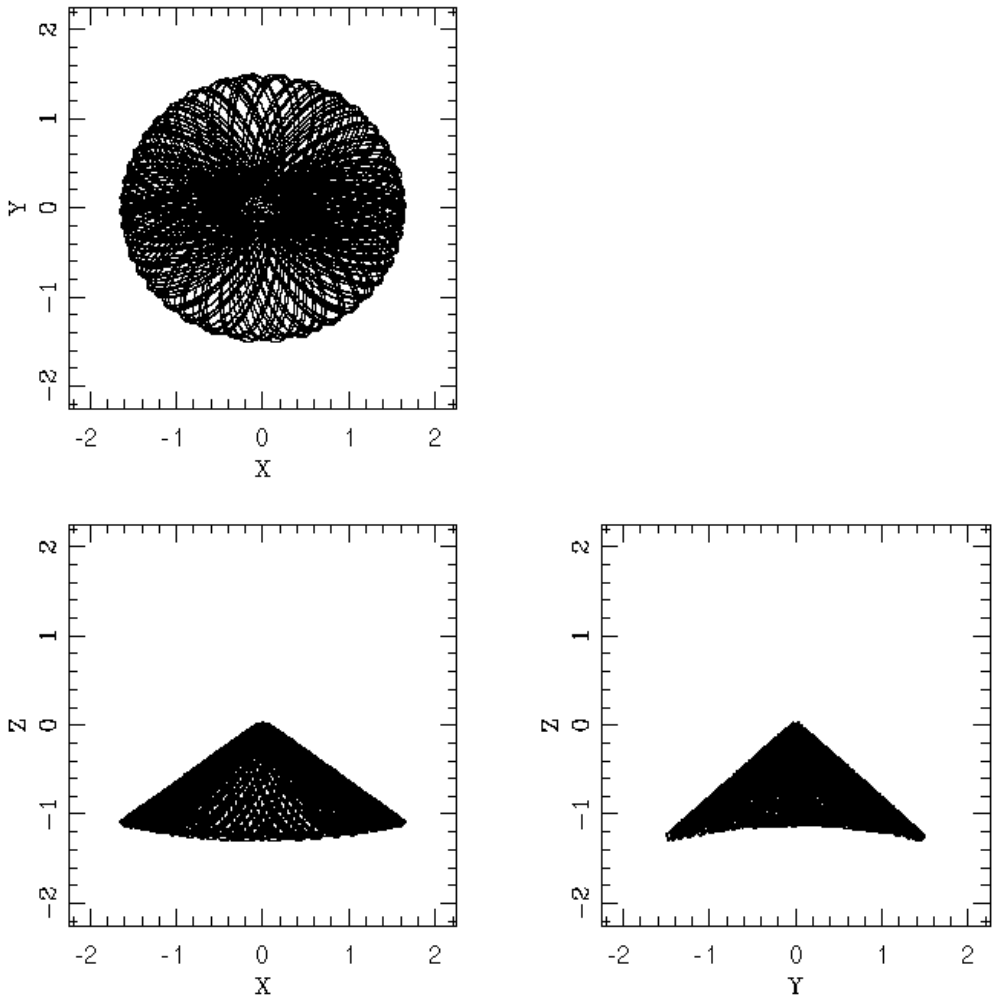

Fig. 7. Real space projections of the $\ell - g$ FPO in oblate triaxial potential. $b_\varphi = 0.99$, $c_\varphi = 0.96$ and energy $E = 2.48$

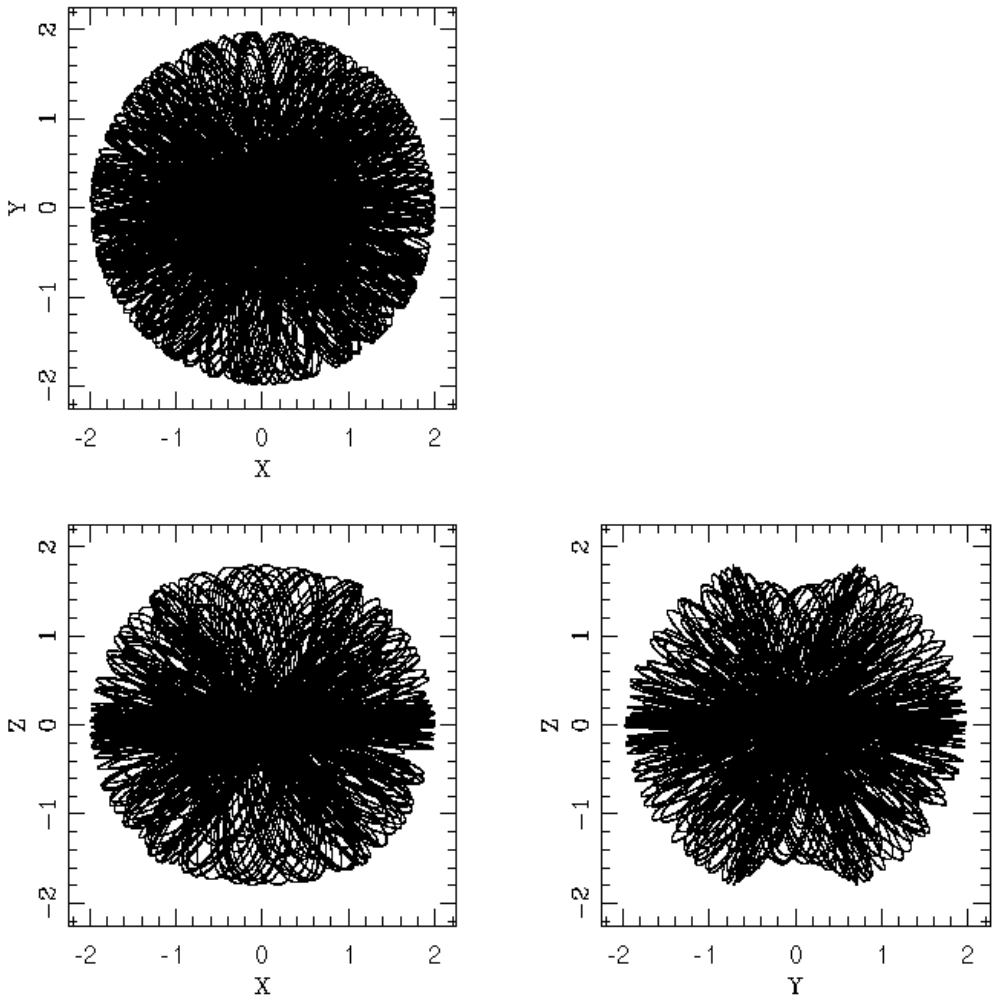

Fig. 8. Real space projections of the separatrix orbit in the oblate triaxial case. $b_\varphi = 0.99$, $c_\varphi = 0.96$ and energy $E = 2.48$

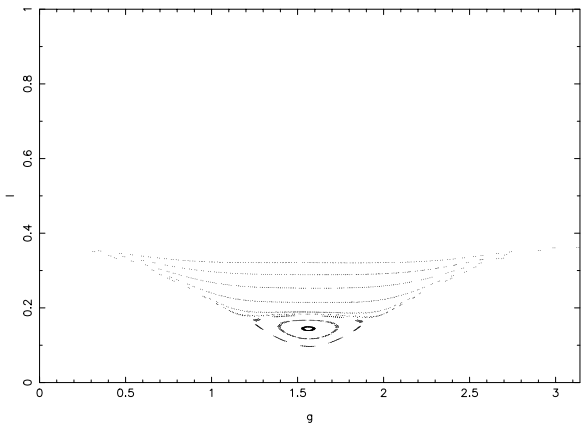

Fig. 9a. $\ell - g$ surface–of–section (strobed at $h = 0$) for prolate triaxial potential. $b_\varphi = 0.99$, $c_\varphi = 1.04$ and energy $E = 2.3$

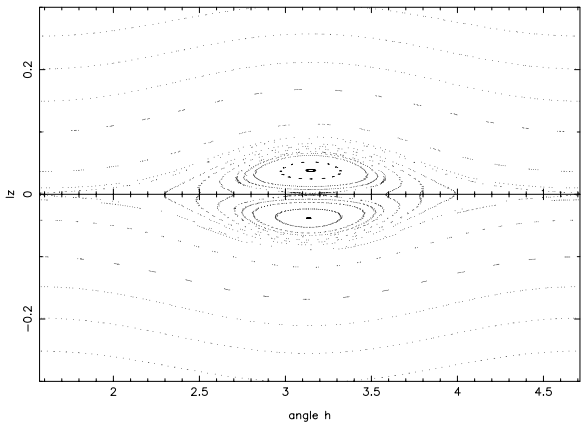

Fig. 9b. $\ell_z - h$ surface–of–section (strobed at $g = \pi/2$) for prolate triaxial potential. $b_\varphi = 0.99$, $c_\varphi = 1.04$ and energy $E = 2.3$

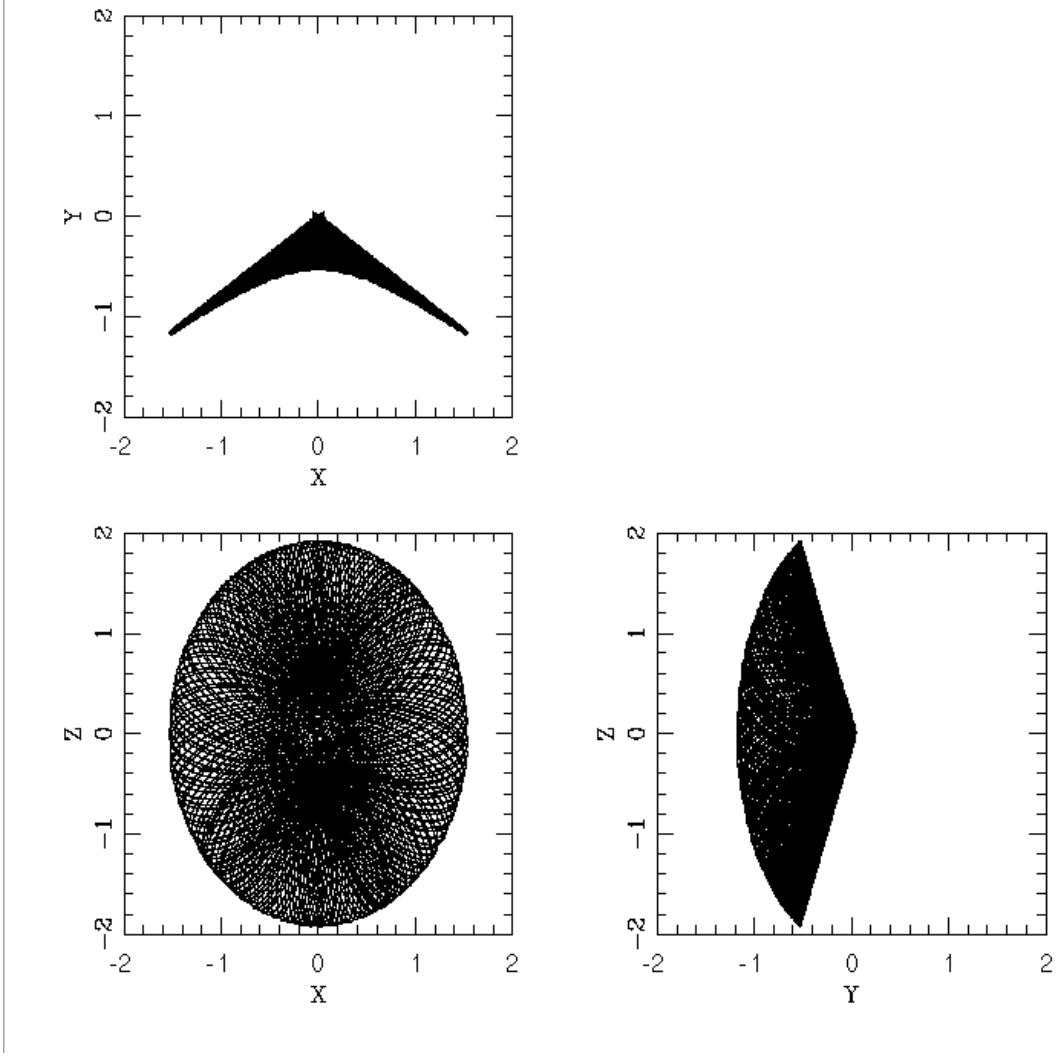

Fig. 10. Real space projections of the $\ell - g$ FPO in prolate triaxial potential. $b_\varphi = 0.99$, $c_\varphi = 1.04$ and energy $E = 2.3$

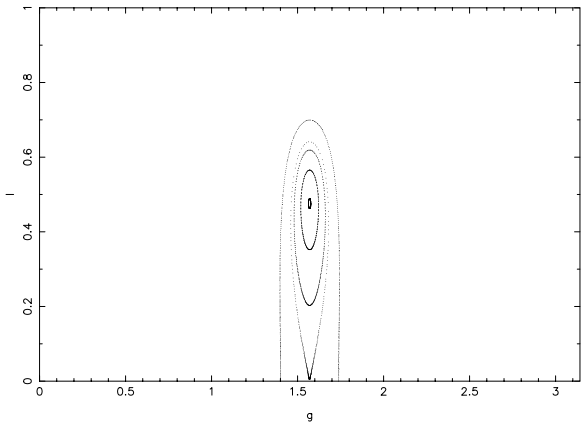

Fig. 11. $\ell - g$ surface–of–section (strobed at $h = \pi/2$) for prolate triaxial potential. $b_\varphi = 0.99$, $c_\varphi = 2.5$ and energy $E = 0.5$

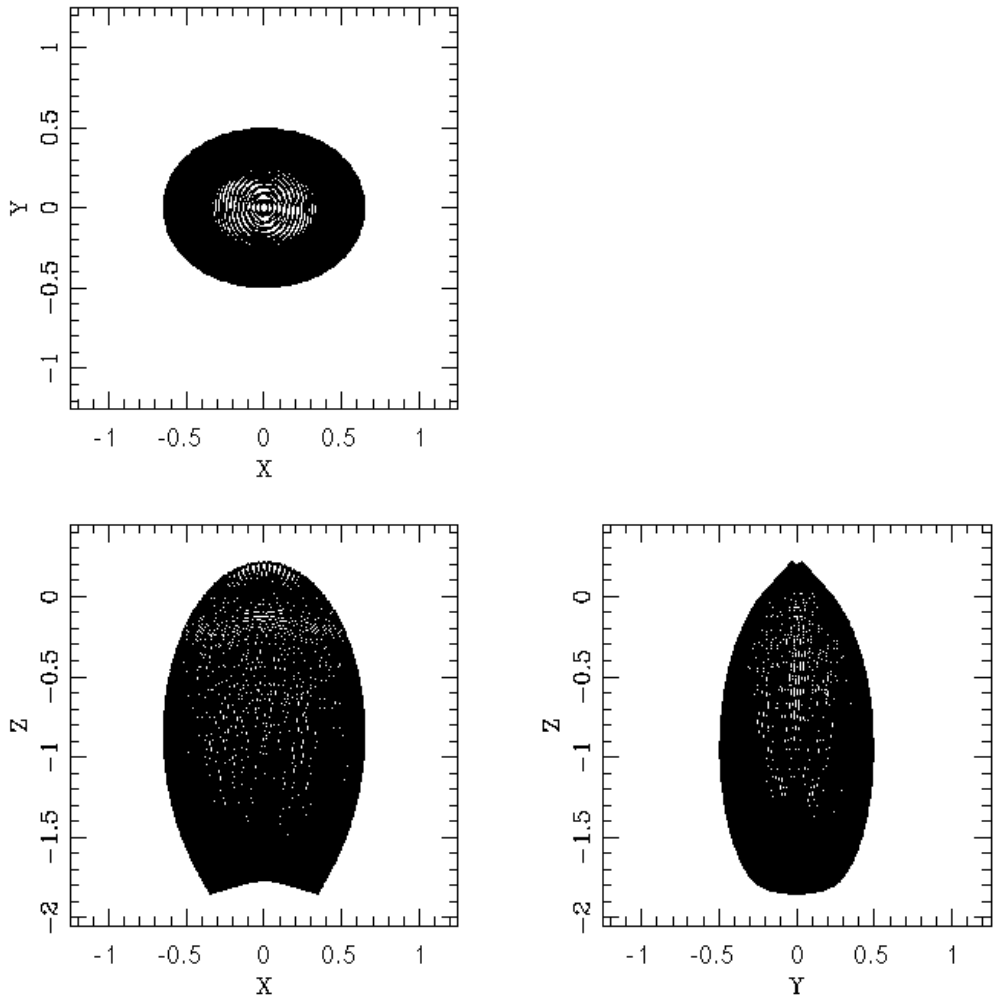

Fig. 12. Real space projections of the $\ell - g$ FPO in prolate triaxial potential. $b_\varphi = 0.99$, $c_\varphi = 2.5$ and energy $E = 0.5$

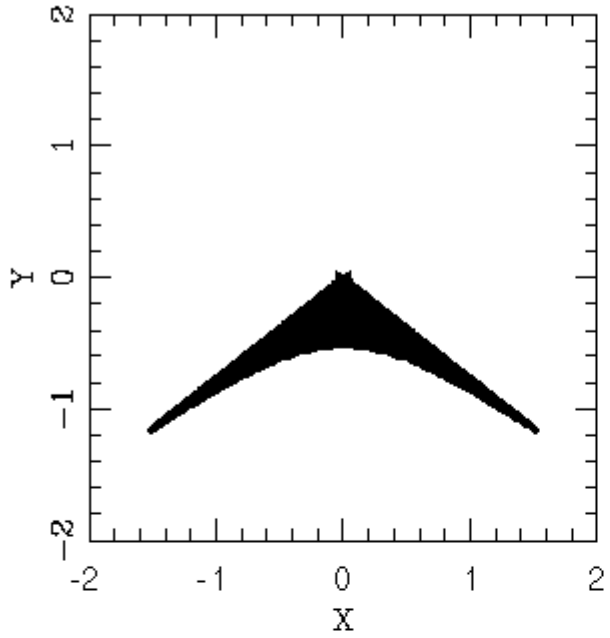
Y
X
2
1
0
−1
−2
-2
-1
0
1
2

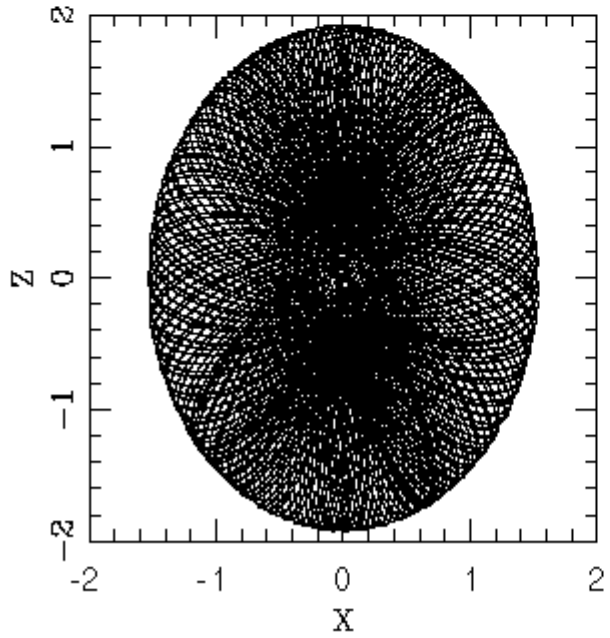
Z
X
2
1
0
−1
−2
-2
-1
0
1
2

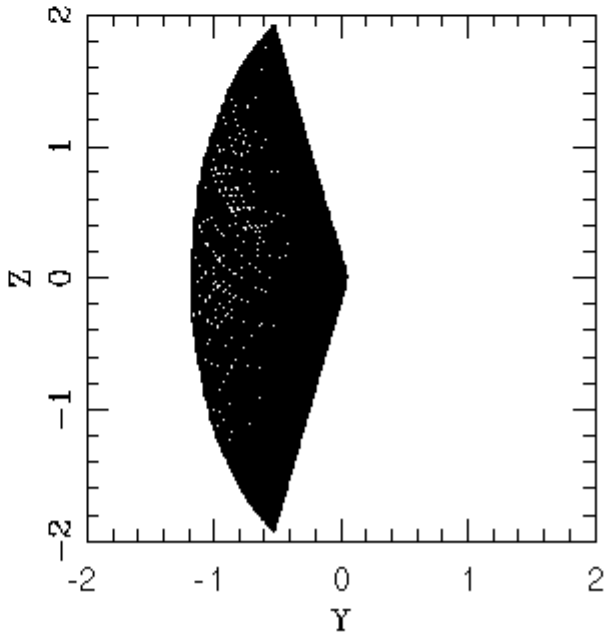
Z
Y
2
1
0
−1
−2
-2
-1
0
1
2

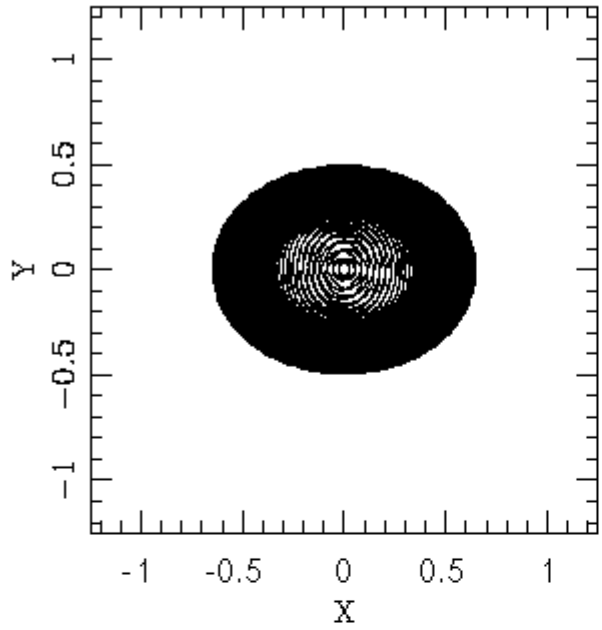
Y
X
1
0.5
0
-0.5
-1
-1
-0.5
0
0.5
1

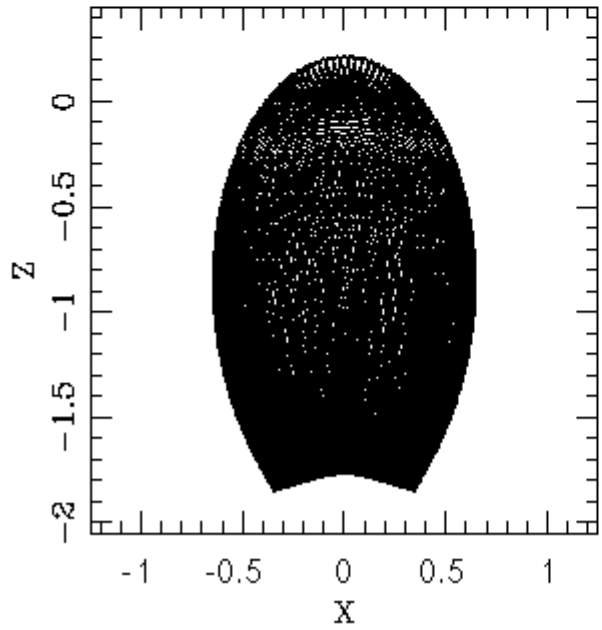
Z
X
0
-0.5
-1
-1.5
-2
-1
-0.5
0
0.5
1

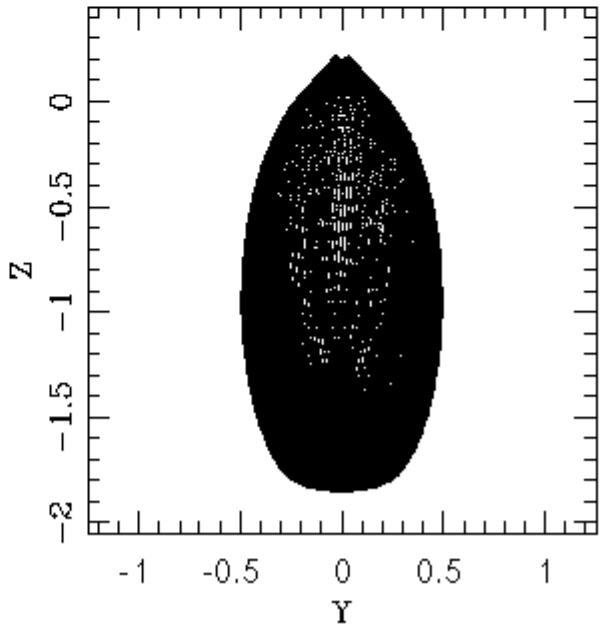
Z
Y
0
-0.5
-1
-1.5
-2
-1
-0.5
0
0.5
1

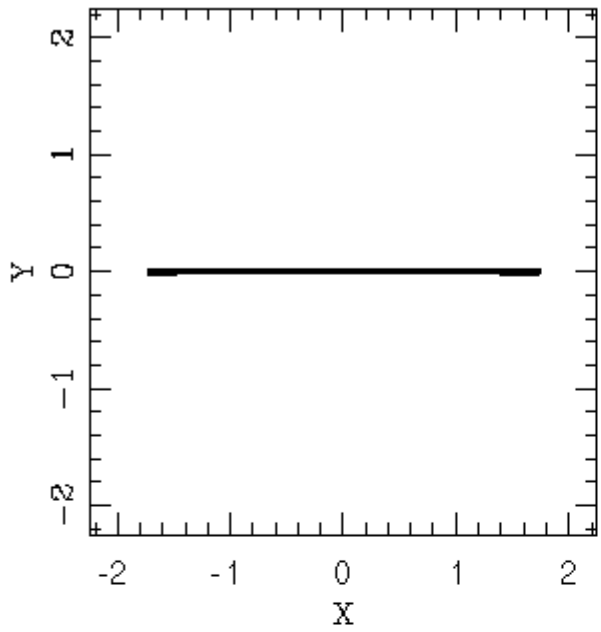
Y
X
-2
-1
0
1
2

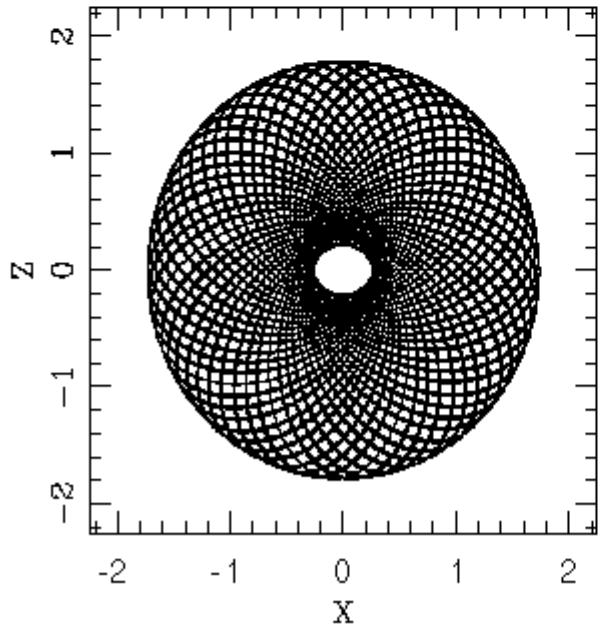
Z
X
-2
-1
0
1
2

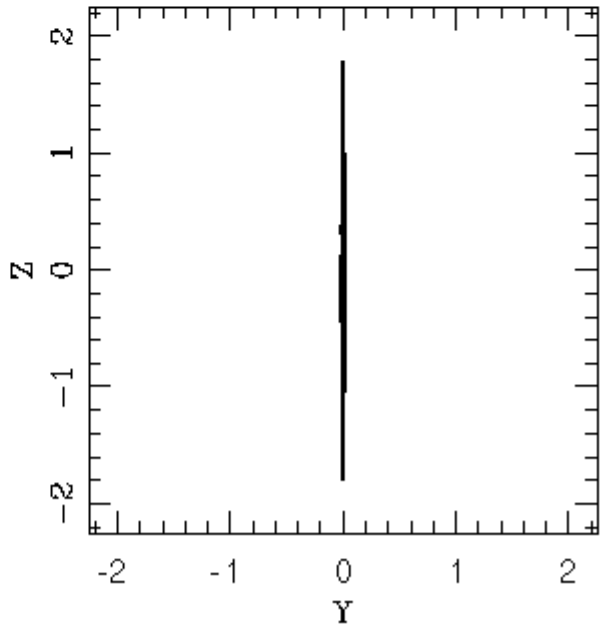
Z
Y
-2
-1
0
1
2

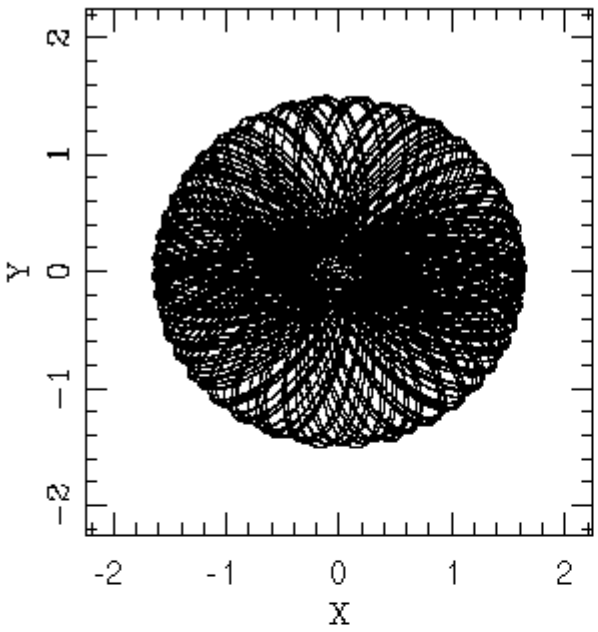
Y
X
-2
-1
0
1
2

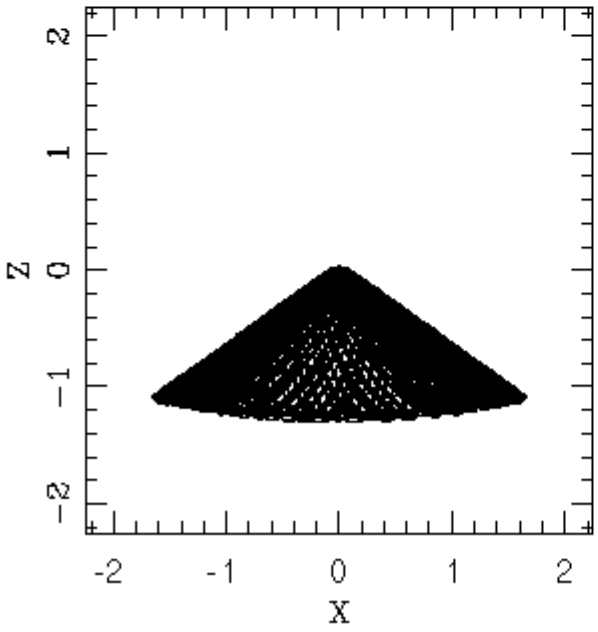
Z
X
-2
-1
0
1
2

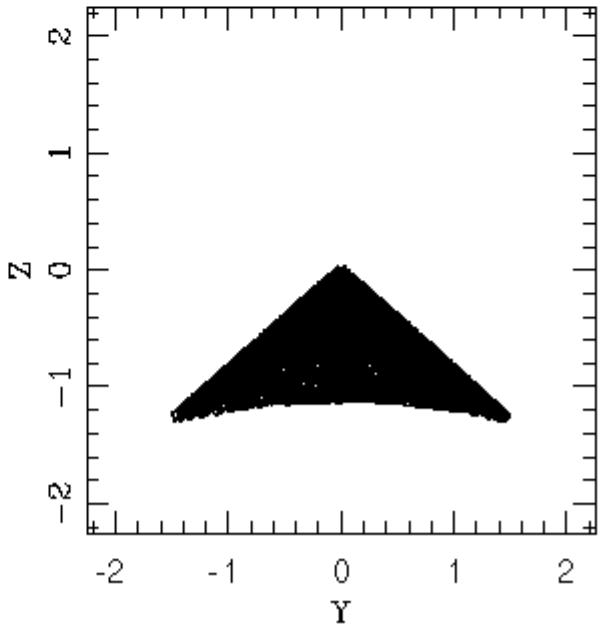
Z
Y
-2
-1
0
1
2

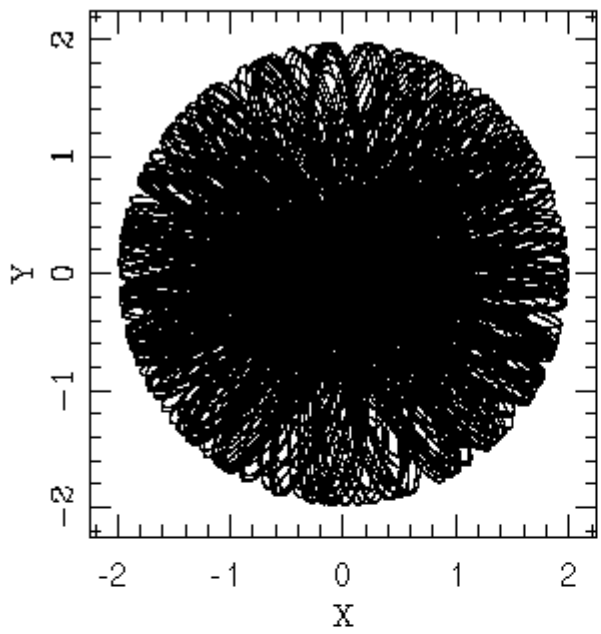
Y
X
-2
-1
0
1
2

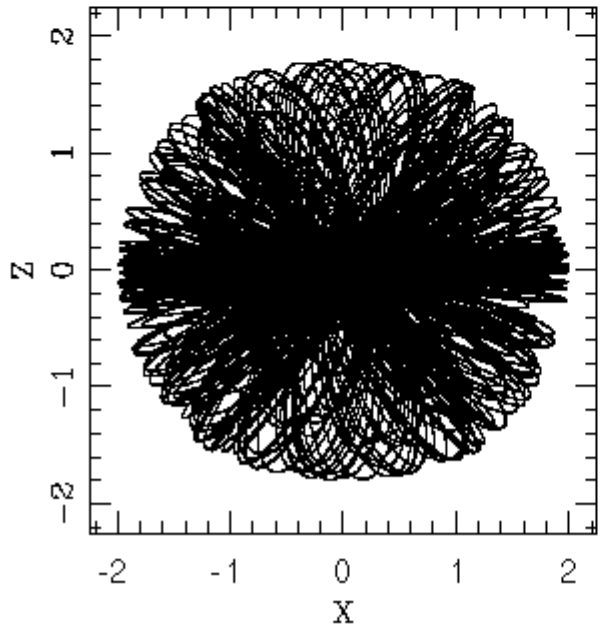
Z
X
-2
-1
0
1
2

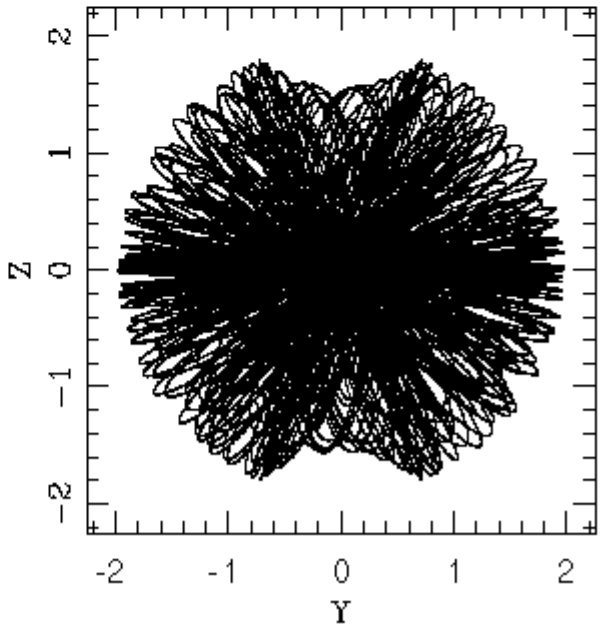
Z
Y
-2
-1
0
1
2